Recalibration of the Hα surface brightness–radius relation for planetary nebulae using Gaia DR3: new distances and the Milky Way oxygen radial gradient

Oscar Cavichia [ID],[1] Hektor H. Monteiro [ID],[1] Adalberto R. da Cunha-Silva,[1] Walter J. Maciel [ID],[2] and André F. S. Cardoso [ID][1, 3]

[1]*Instituto de Física e Química, Universidade Federal de Itajubá*
Av. BPS, 1303, 37500-903, Itajubá-MG, Brazil
[2]*Instituto de Astronomia, Geofísica e Ciências Atmosféricas, Universidade de São Paulo*
Rua do Matão, 1226, 05508-090, São Paulo-SP, Brazil
[3]*Núcleo Cosmo-Ufes & Departamento de Física – Universidade Federal do Espírito Santo*
29075-910, Vitória, ES, Brazil

ABSTRACT

The spatial distribution of chemical elements in the Galactic disk provides key constraints on models of galaxy evolution. However, studies using planetary nebulae (PNe) as tracers have been historically limited by large uncertainties in their distances. To overcome the long-standing distance uncertainties, we recalibrated the Hα surface brightness–radius relation (Frew et al. 2016) with *Gaia* DR3 parallaxes, deriving statistical distances for 1,200 PNe and Bayesian distances for 419 objects with reliable parallaxes. Adopting Bayesian values preferentially, we determined the O/H radial gradient for 230 disk PNe. We tested three models: a single linear gradient, a segmented fit with one break, and a segmented fit with two breaks. Although model selection is statistically inconclusive, segmented fits indicate a change in slope near the solar radius ($R \sim 8$ kpc), with a flatter or slightly positive gradient inward and a steeper negative gradient outward. This feature may reflect changes in star formation efficiency driven by the Galactic bar or the corotation resonance of the spiral arms. Comparison with other tracers—Cepheids, red giants, and open clusters—shows qualitative consistency. The two-dimensional O/H distribution in the Galactic plane supports the adopted distances and reveals modest azimuthal asymmetry, with enhanced abundances near the bar at positive longitudes, and a bimodal abundance structure between the inner and outer solar regions. Our results provide new constraints on the chemical evolution of the Milky Way, the impact of non-axisymmetric structures, and the possible existence of distinct radial abundance regimes across the Galactic disk.

Keywords: Planetary nebulae (1249) — Chemical abundances (224) — Milky Way disk (1050) — Galaxy chemical evolution (580)

1. INTRODUCTION

The absolute amount of metals, the relative abundance of different elements, and their spatial distributions in a galaxy directly depend on the galactic evolutionary history and, therefore, serve as crucial constraints for chemical evolution models (Gibson et al. 2013). In this context, the radial gradient of chemical abundances in the disks of spiral galaxies is one of the most important constraints for galaxy chemical

Email: cavichia@unifei.edu.br

evolution models (Henry & Worthey 1999). The gradient was first observed in the Milky Way by Shaver et al. (1983), revealing a radial decrease in oxygen abundances, with higher values in the central regions. Subsequently, the abundance gradient was observed in other external galaxies, as shown in McCall et al. (1985), Zaritsky et al. (1994), and Vila-Costas & Edmunds (1992), and is now well-established in the local universe (Sánchez et al. 2014). Currently, a typical gradient of ~ -0.05 dex/kpc is found for the Milky Way disk (Mollá et al. 2019). This gradient results from various physical processes acting from galaxy formation to the present,

including gas infall/outflow, stellar formation history, initial mass function, and radial gas flows. Gibson et al. (2013) demonstrated that the existence and evolution of these gradients strongly depend on the prescriptions for star formation and gas infall included in the simulations. While recognizing the concurrence of observations for a negative gradient in the radial interval of galactocentric distances $4 \lesssim R \lesssim 10$ kpc in the Milky Way disk and 0.5 to $2R_{\mathrm{e}}$ in other spiral galaxies, where R_{e} is the effective radius (half-light radius), there are evidences of a flattening of the gradient in spiral galaxies beyond $2R_{\mathrm{e}}$ (Sánchez et al. 2014; Sánchez-Menguiano et al. 2016). The advent of multi-object and integral field spectroscopy has ushered in instruments with expansive fields of view, enabling a new generation of surveys focused on the observation of H II regions in external galaxies. Surveys like CALIFA (Sánchez et al. 2012) and MANGA (Bundy et al. 2015) have extensively observed hundreds of H II regions in the disks of nearby spiral galaxies, providing comprehensive 2D coverage. The results presented by Sánchez et al. (2014), based on observations of over 7000 H II regions in 306 spiral galaxies, indicate evidence of a flattening of the O/H gradient beyond $2R_{\mathrm{e}}$, consistent with earlier studies focusing primarily on a few objects (e.g., Bresolin et al. 2009). These findings were further supported by Sánchez-Menguiano et al. (2016).

In the case of the Milky Way, a significant debate exists in the literature regarding the constancy of the gradient for different galactocentric distances. In the outer regions of the Milky Way ($R > 10$ kpc) a flattening of the radial gradient of the disk is noted by data from different tracers such as open clusters (Lépine et al. 2011; Monteiro et al. 2021; Magrini et al. 2023), H II regions (Esteban et al. 2013), Cepheid stars (Genovali et al. 2014; Minniti et al. 2020), and planetary nebulae (PNe, Maciel & Costa 2009; Stanghellini & Haywood 2018). The findings from these studies indicate that abundances remain relatively constant in the outer disk as R increases. However, there are discrepancies in the literature regarding these results, as evidenced by studies such as Fernández-Martín et al. (2017); Esteban et al. (2017); Arellano-Córdova et al. (2020); Méndez-Delgado et al. (2022) for H II regions, and Stanghellini & Haywood (2010); Pagomenos et al. (2018) and Bucciarelli & Stanghellini (2023, hereafter BS23) for PNe, where the gradient is suggested to maintain the same slope across the entire optical disk. On the other hand, Henry et al. (2010) analyzed disk PNe data to derive the radial gradient and find evidence suggesting a steepening of the gradient at large Galactocentric distances.

However, they emphasize the need for additional data to confirm this result.

Due to discrepancies within the literature, establishing whether the gradient maintains a consistent slope across all observed radii in the Milky Way proves challenging. Part of the disparity between different studies stems from uncertainties in determining chemical abundances and/or distances. Estimating reliable distances for Galactic PNe proves particularly challenging, as no single physical parameter directly depends on the distance. Statistical distance methods have therefore been developed to derive PNe distances (see Frew et al. 2016, hereafter F16, for a comprehensive review). The statistical distance scale from F16, based on an empirical relation between $H\alpha$ surface brightness ($S_{H\alpha}$) and the intrinsic radius of the PNe, has made an important improvement in the determination of PNe distances. This relation was calibrated using data for 322 PNe, of which 206 are Galactic and 126 are extragalactic objects. They provide three relations, one for the full sample, one for optically thick objects, and one for optically thin PNe. Distances for 1133 PNe are given, 515 of them being classified as optically thick or optically thin nebulae.

However, statistical distances are subject to considerable uncertainties, often due to factors of two or more, as discussed by F16. Consequently, trigonometric techniques remain the direct and reliable individual method to determine the distances of the PNe when the parallax errors are small (parallax uncertainty over parallax, σ_{ϖ}/ϖ, lower than 0.15, Hernández-Juárez et al. 2024). In this regard, the recent *Gaia* mission (Gaia Collaboration et al. 2016, 2018) has revolutionized the determination of the distances for the Galactic PNe (González-Santamaría et al. 2021; Chornay & Walton 2021). Before *Gaia*, only a dozen of PNe located very close to the Sun had distances estimated from parallaxes (F16). *Gaia* has significantly altered this by providing precise parallaxes for hundreds of Galactic PNe. The identification of PNe in *Gaia* archive has been improved in the last few years. Stanghellini et al. (2017) identified 8 central stars of PNe (CSPNe) in the DR1. Kimeswenger & Barría (2018) have manually identified 382 *Gaia* sources in DR2 that match the PNe coordinates. Stanghellini et al. (2020) matched the astrometry of CSPNe with DR2 finding 430 sources. Ali et al. (2022) matched *Gaia* sources with the HASH catalog (Parker et al. 2006) and Weidmann et al. (2020) CSPNe coordinates finding 603 sources in common. González-Santamaría et al. (2021) and Chornay & Walton (2020, 2021) developed more sophisticated methods based on the color and geometric distance of the *Gaia* sources in EDR3 to identify 2035 and 2000 PNe correspondences, respectively.

The *Gaia* DR3 (Gaia Collaboration et al. 2016, 2023b) provides unprecedented astrometric parameters, complemented by photometric and spectroscopic data, for hundreds of CSPNe. Even after *Gaia* observations, statistical distances for PNe will be continuously used, since many PNe will not have *Gaia* distance estimates because of the CSPNe are not well identified or in the cases where the parallaxes have a considerable error. In this regard, statistical distance methods for PNe have been recalibrated by using *Gaia* astrometric data, as demonstrated by Stanghellini et al. (2020); Ali et al. (2022) and BS23.

In this paper, our aim is to revisit the issue of PNe abundance gradients relying on reliable distances determined directly from astrometric parallaxes provided by Gaia data and from statistical distance scale. We present a recalibration of the PN distance scale from F16 using the best parallaxes available from *Gaia* DR3 (Lindegren et al. 2021), enhancing its ability as a robust distance indicator for the many PNe which will not have *Gaia* distance estimates.

This work is organized as follows: in Section 2 the source selection from the *Gaia* DR3 data, the adopted chemical abundances, the adopted methodology to derive the PNe distances, and the criterion to separate the thin and thick disk samples are presented. In Section 3 the main results are described related with the radial and azimuthal oxygen abundances distribution and in Section 4 the discussion and conclusions are presented.

2. METHODS

2.1. *Gaia DR3 source identification*

The *Gaia* space mission was launched and operated by the European Space Agency (ESA) to provide a detailed three-dimensional map of the Milky Way Galaxy. The *Gaia* data release (*Gaia* DR3) was published in June 2022 and provides full astrometric solution — positions on the sky (α, δ), parallaxes (ϖ), and proper motions (μ) — for around 1.46 billion sources, G magnitudes for around 1.806 billion sources, G_{BP} and G_{RP} magnitudes for around 1.54 billion and 1.55 billion sources, respectively. Compared to *Gaia* DR2, the new release offers significant improvements in astrometric and photometric accuracy, precision, and homogeneity (Gaia Collaboration et al. 2023b).

The identification of *Gaia* sources that match the CSPNe has demonstrated to be challenge, as the CSPNe are faint and sometimes undetectable, or may have multiple candidate sources within the central region of the nebula. González-Santamaría et al. (2021) developed a method to identify CSPNe in *Gaia* EDR3 based on proximity to the geometric center of the nebula and photometric color. Similarly, Chornay & Walton (2020) and

Chornay & Walton (2021, hereafter CW21) employed a likelihood ratio method to cross-match known PNe with *Gaia* EDR3 sources, using empirically derived positional and color distributions to assess candidate likelihoods. We adopted a procedure in this paper similar to González-Santamaría et al. (2021) but with some enhancements as detailed below.

We began by constructing a catalog of PNe coordinates. Whenever available, CSPNe coordinates were taken from Weidmann et al. (2020); otherwise, we used our internal PNe database (Maciel et al. 2015) and coordinates from Frew et al. (2013), F16, and CW21. Angular diameters were preferentially adopted from F16, supplemented by data from Tylenda et al. (2003), Stanghellini et al. (2008), and Acker et al. (1992). This compilation resulted in a sample of 1,200 PNe with reliable coordinates and angular diameters.

We queried the *Gaia* archive around the compiled coordinates, setting the search radius from half the nebular radius up to a maximum of 80% of the radius. For cases where half the nebular radius was less than $1.8''$, we used this value as the minimum radius, following the *Gaia* documentation formula: $1'' + \Delta_{\mathrm{epoch}}, [\mathrm{yr}] \times 0.050''/\mathrm{yr} = 1.8''$, where $\Delta_{\mathrm{epoch}} = 2016 - 2000 = 16$ yr and $0.050''/\mathrm{yr}$ corresponds to the maximum expected proper motion for 99.8% of *Gaia* sources. In addition, it is essential to assess the quality of the astrometric solutions. This is commonly evaluated using the Renormalized Unit Weight Error (RUWE) parameter, which quantifies the goodness-of-fit of the astrometric model to the observations (Lindegren et al. 2018). RUWE values greater than 1.4 typically indicate unreliable or problematic astrometric solutions.[4] In this work, we exclude parallaxes from sources with RUWE > 1.4 and applied the condition `visibility_periods_used` > 8 to ensure reliable astrometric solutions. This search yielded 27,401 *Gaia* sources for the 1,200 PNe in our database. As an additional and necessary step, parallaxes were corrected for the zero-point offset following the prescription of Lindegren et al. (2021).

To identify the most probable CSPNe, we implemented the color-distance method of González-Santamaría et al. (2021). We assumed a minimum CSPN temperature of 13,000 K for the post-AGB transition phase (Weidmann et al. 2020), and applied the color–temperature relation from Jordi et al. (2010), where $G_{\mathrm{BP}} - G_{\mathrm{RP}} = -0.2$ corresponds to $T_{\mathrm{eff}} = 14,477$ K, establishing this value as the upper color limit for candidate selection. For sources lacking $G_{\mathrm{BP}} - G_{\mathrm{RP}}$ col-

---

[4] See the *Gaia* technical note GAIA-C3-TN-LU-LL-124-01 and documentation at https://www.cosmos.esa.int/web/gaia/dr3.

ors but with available $T_{\rm eff}$ from DR3, we used the inverse relation from Jordi et al. (2010) to estimate the corresponding color.

To further refine the selection, we used the `astropy` package (Astropy Collaboration et al. 2022) to account for proper motion of the *Gaia* sources and calculate coordinates at the reference epoch J2000. Interstellar extinction corrections were applied to the photometry using the Bayestar (Green et al. 2019), Marshall (Marshall et al. 2006), and SFD (Schlegel et al. 1998) extinction maps, in that order of priority. Visual extinctions were converted to *Gaia* band extinctions using the relations provided by Gentile Fusillo et al. (2021).

We adopted the classification scheme from González-Santamaría et al. (2021), grouping the identifications into three reliability classes: A (most reliable), B, and C (least reliable). In our sample, 48% of the CSPNe fell into group A, 36% into group B, and 16% into group C. This represents a notable improvement over González-Santamaría et al. (2021), who report 31.6%, 30.9%, and 37.5% in groups A, B, and C, respectively.

We then cross-matched our high-confidence identifications with those from CW21, selecting their "true" PNe with reliability scores > 0.8. This yielded 462 PNe in common. As an additional consistency check, we compared the visual extinction values derived for each PN from the Balmer decrement reported in F16 with the extinction from Galactic dust maps, as shown in the left panel of Fig.1. While the agreement is generally good, some outliers deviate significantly from the identity line, suggesting either incorrect CSPN associations, non-standard extinction values, or PNe with high internal dust content. We excluded sources lying more than 3σ from the identity relation, as illustrated in the right panel of Fig.1. Our final sample consists of 419 PNe with a high probability of correct association between the *Gaia* sources and their corresponding CSPNe.

2.2. *Distances*

The Hα surface brightness–radius relation was used by F16 to obtain statistical distances for Galactic PNe. The scale was calibrated based on a large number of PNe from our Galaxy as well as other nearby galaxies. To perform the calibration, the distances were determined by several different methods, including a small number of 13 PNe with precise trigonometric parallaxes and also other less reliable distances, including photometric distances, eclipsing binaries, expansion parallaxes, physical membership of a PN in an open or globular star cluster, Galactic bulge or a galaxy, among others (see F16, for more details). *Gaia* DR3 data allow a recalibration of the Hα surface brightness–radius relation obtained by
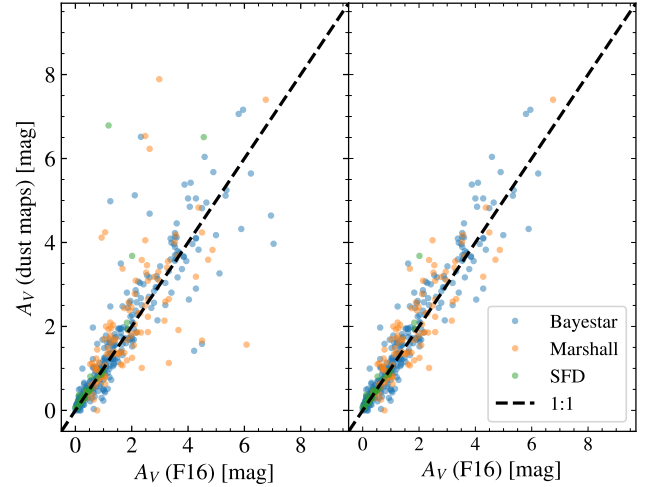
Figure 1. Left: extinction in the visual band obtained in this work from the Bayestar (Green et al. 2019), Marshall (Marshall et al. 2006) and SFD (Schlegel et al. 1998) dust maps as a function of the extinction obtained from F16, as labeled. Right: the same as the right panel but excluding PNe that are 3σ from the identity line.

F16, as a large number of PNe have accurate astrometric parallaxes are available.

2.2.1. *Recalibration of the Hα surface brightness–radius relation*

PNe with accurate parallaxes can be used to recalibrate the Hα surface brightness–radius relation obtained by F16. In the cases where the fractional parallax uncertainties are low, it is possible to calculate the physical radius of the PN using $R_{\rm pc} = \theta/(206265 \times \varpi)$, where θ is the PN angular radius in arcsec. The intrinsic Hα surface brightness in units of $\rm erg\,cm^{-2}\,s^{-1}\,sr^{-1}$ is calculated using the formula $S_{\rm H\alpha} = F_{\rm H\alpha}/(4\pi\theta^2)$, being that $F_{\rm H\alpha}$ the Hα flux and θ the angular diameter, both obtained from F16.

We tested the effects of selecting different parallaxes precision by selecting the PNe with fractional parallax uncertainties $f = \sigma_\varpi/\varpi$ lower than 0.05, 0.10, 0.15 and 0.20. The results are displayed in Fig. 2, where the data are color-coded by the ionized mass, calculated from the Hα fluxes using the equation provided by F16. In the same figure we plotted the F16 relation obtained from their full sample of 322 PNe. We performed a linear fit for each of the relations and the resulting parameters are summarized in Table 1. In this table, the first column corresponds to the fractional parallax uncertainty, the second column the number of calibrators, the third and fourth columns the slope and the intercept of the linear fit with the respective errors, and the fifth column the Pearson correlation coefficient. We also indicate in
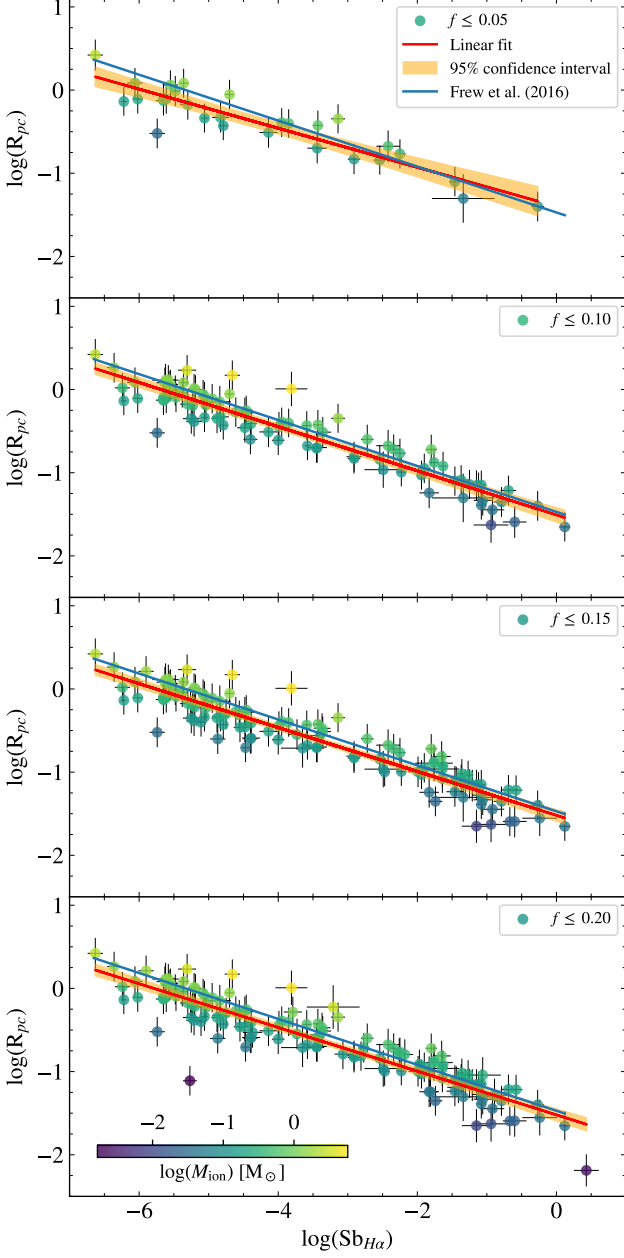
Figure 2. Recalibration of the Hα surface brightness–radius relation based on *Gaia* DR3 parallaxes and considering different fractional parallaxes uncertainties f, as labeled. The red line and the orange shaded region represent the linear fit and the 95% confidence interval, respectively. The blue line represent the linear fit obtained by F16 for reference. The data are color-coded by the ionized mass (see the text for details).

the table the averaged distance ratio $\langle k \rangle$, which consists in the average of the statistical distance multiplied by the parallax, $\langle k \rangle = \langle D_{\text{stat}} \times \varpi \rangle$, and its dispersion $\langle \sigma \rangle$, which is an indicator of the goodness of the scale (see Smith 2015). As presented in Fig. 2, independently

of the adopted fractional parallax uncertainty, the linear fits obtained using *Gaia* data are slightly flatter than the obtained from F16, considering the 95% confidence interval. This implies in shorter final statistical distances when using our calibrated relation. It can also be seen in the figure that for $f = 0.20$ there exists PNe with $\log(M_{\text{ion}}) < -2$, which are outliers from the linear relation. This was identified by Stanghellini et al. (2020) and also confirmed by BS23.
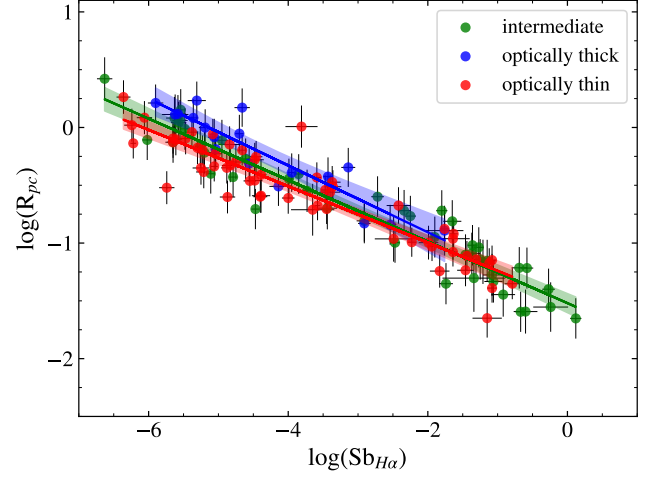
Figure 3. The Hα surface brightness–radius relation based on *Gaia* DR3 parallaxes and classifying the PNe according to the optical depth. The data and the lines are color-coded for optically thin, thick and intermediate cases, as labeled. The lines and the shaded regions represent linear fits and the 95% confidence intervals for each sub-class. The data are restricted to parallaxes uncertainties $f \leq 0.15$.

As given in Table 1, the fitted parameters presented are compatible with each other, given the errors. The flatter relation is obtained for $f = 0.05$, with only 29 calibrators. In this case the correlation coefficient is lower as in the case of $f = 0.20$ but with 138 calibrators. We consider that the cases $f = 0.10$ and $f = 0.15$ provide better fits, with slightly larger correlation coefficients, compatible with those obtained by F16. However, $f = 0.15$ provides lower $\langle \sigma \rangle$, with a similar averaged distance ratio and with 121 calibrators. Therefore, we will consider the case $f = 0.15$ as the best fitted scale and the adopted Hα surface brightness–radius relation as:

$$\log R_{\text{pc}} = (-0.26 \pm 0.03) \times \log S_{\text{H}\alpha} - (1.52 \pm 0.03). \quad (1)$$

F16 also notice a dependence of the Hα surface brightness–radius relation with the optical depth, resulting in optically thick PNe tending to populate the upper bound of the trend, while optically thin PNe falling along the

Table 1. Parameters of the scales.

f	$N_{\rm cal}$	slope	intercept	r	$\langle k \rangle$	$\langle \sigma \rangle$
(1)	(2)	(3)	(4)	(5)	(6)	(7)
			All			
0.05	29	-0.23 ± 0.09	-1.40 ± 0.09	-0.92	1.080	0.155
0.10	88	-0.27 ± 0.04	-1.51 ± 0.04	-0.94	1.079	0.392
0.15	121	-0.26 ± 0.03	-1.52 ± 0.03	-0.94	1.084	0.299
0.20	138	-0.26 ± 0.04	-1.52 ± 0.04	-0.92	1.134	0.502
			intermediate			
0.15	46	-0.27 ± 0.04	-1.52 ± 0.04	-0.96	1.066	0.296
			optically thin			
0.15	58	-0.24 ± 0.05	-1.48 ± 0.05	-0.93	1.074	0.504
			optically thick			
0.15	18	-0.29 ± 0.14	-1.48 ± 0.14	-0.92	1.049	2.570

lower boundary in the $S_{\rm H\alpha} - R_{\rm pc}$ plane. We follow F16 and use the same classification as they use for optically thick and optically thin PNe, based on the intensity of the spectroscopic lines. Fig. 3 shows the Hα surface brightness–radius relation but for PNe separated in optically thin, optically thick and intermediate cases and considering the fractional parallax uncertainty $f \leq 0.15$. We also performed linear straight line fits and the results are reported in Table 1, as indicated. The differences in the slopes for the three classifications are within the errors, but generally the results agree with F16. Optically thin PNe show a flatter slope and the slope for the optically thick PNe is steeper. However, as the number of calibrators is not high for each classification, specially for optically thick PNe, we prefer to use the linear relation for all PNe as presented in equation 1 and let the division by optical depth based on *Gaia* data for future studies with larger datasets.

2.2.2. *Bayesian distances*

While the recalibration of the Hα surface brightness–radius relation is important to obtain statistical distances for a large set of PNe in the Galaxy, more reliable distances can be obtained for PNe using a probabilistic approach. Bailer-Jones et al. (2021) estimated stellar distances using a prior constructed from a three-dimensional model of our Galaxy. Their model includes interstellar extinction and *Gaia* variable magnitude limit and inferred two types of distances. The geometric uses the parallax with a direction-dependent prior on distance. The photogeometric, additionally uses the color and apparent magnitude of a star, by exploiting the fact that stars of a given color have a restricted range of probable absolute magnitudes. The geometric distances are very dependent on the Galaxy model adopted, while photogeometric distances depend

on a model of the direction-dependent distribution of extincted stellar absolute magnitudes. The application of this method to PNe is very uncertain, since CSPNe have a wide range of properties, with temperatures ranging from $\sim 25,000$ to over $200,000$ K, luminosities from 10 to over $10,000$ $L_{\odot}$, and a great variety of spectra (Weidmann et al. 2020).

The best approach for PNe is to derive distances based on a Bayesian statistics, using the statistical distances and its uncertainty as a prior $P^*(r)$, as in CW21, where they used the statistical distances from F16 as a prior to derive Bayesian distances and using *Gaia* EDR3 parallaxes. We will proceed as CW21, but instead we will use our recalibration of the Hα surface brightness–radius relation based on *Gaia* DR3 data to derive more reliable distances for the PNe in our sample. Additionally, the *Gaia* parallax ϖ and its uncertainty σ_ϖ provide the likelihood.

To estimate the uncertainty, Bailer-Jones (2015) recommends to use 5% and 95% quantiles to define the 90% confidence interval of the posterior distribution. However, as Frew et al. (2016) present the uncertainties using 68% confidence interval, we adopted this procedure. Also, following Bailer-Jones et al. (2021), the distances are adopted as the median and, because many of our posteriors are not well approximated as Gaussian, a Markov-Chain Monte Carlo (MCMC) algorithm was implemented to compute the posterior distance distribution, sampling the parameter space with 10,000 samples. The results for three PNe are displayed in Fig. 4 as examples of the resulted distributions.

Comparisons of the obtained distances following this method are presented in Fig. 5, where in the top panel a comparison with CW21 is provided. CW21 distances are on average 18% higher than our Bayesian distances. We also note the effect of the recalibration of the statistical scale performed in this work, as for PNe closer to the Sun (distances lower than $\sim$1500 pc) the spread in the data considering $\log(D_{\rm CW21}/D_{tw})$ is much lower. F16 distances are on average 33% higher, as can be seen in the bottom panel of the figure. For this case, the Bayesian method also increases the scatter in the distances ratio, as the distances also rely on the trigonometric parallaxes. Therefore, the distances provided in this work are shorter than previous distances based on the Hα surface brightness–radius relation.

### 2.3. *Velocities and halo, thin and thick disk selection criterion*

Some of the *Gaia* DR3 sources have the equatorial proper motions and errors $\mu_{\alpha^*} \pm \sigma_{\mu_{\alpha^*}}$ and $\mu_\delta \pm \sigma_{\mu_\delta}$ provided by the satellite. Combining these proper motions
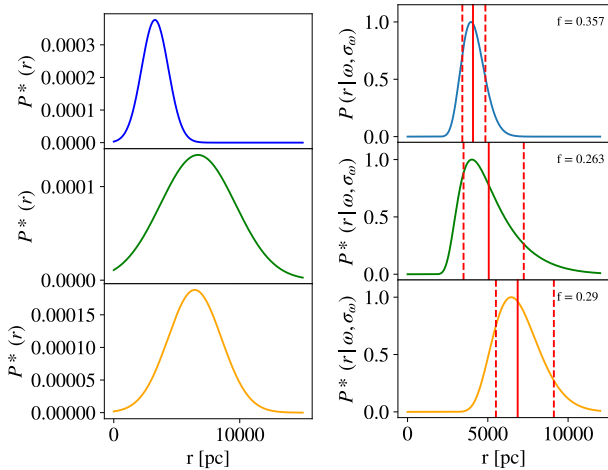
Figure 4. Left panels: unnormalized priors distributions using statistical distances from the Hα surface brightness–radius relation as recalibrated in this work. Right panels: respective unnormalized posterior distributions. The vertical continuous line represents the median and the vertical dashed lines represent the 68% confidence intervals. The three sources have fractional parallax uncertainties f as labeled in the right panels.

with the radial velocities from Durand et al. (1998), we are able to obtain the 3D spacial motions of some PNe in our sample. We proceed as in BS23 to convert the DR3 proper motions and their standard deviations into Galactic coordinates and to compute the corresponding observed spatial velocities plus errors: $V_\ell \pm \sigma_{V_\ell}$ and $V_b \pm \sigma_{V_b}$, where ℓ and b are the Galactic longitude and latitude. The peculiar velocity (V_{pec}) is the residual stellar motion that deviates from the general Galactic rotation. The procedures to obtain V_{pec}, the radial (V_R), azimuthal (V_ϕ) and vertical (V_z) components of the spatial velocity are calculated as in BS23 and we refer the reader to Section 3.2 for more details. In this work we adopt the Sun distance to the Galactic Center $R_\odot = 8.122$ kpc from GRAVITY Collaboration et al. (2018).

As the matching methodology for *Gaia* sources and CSPNe is not the same and also the distances derived in this work are derived from a recalibration of the Hα surface brightness–radius relation and using the Bayesian approach, the velocities derived by us are not exactly the same as those from BS23. In order to select the PNe belonging to the halo and the thin and thick disks, or transitional phases, we constructed the Toomre diagram, as shown in Fig. 6, as in Bensby et al. (2014). Thin disk PNe population have V_{pec} lower than 50 km/s and a thick disk stars with velocities between 70 and 200 km/s. Also, stars with velocities between 50 and 70 km/s are the ones considered to be transitory members between the thin and thick disks.
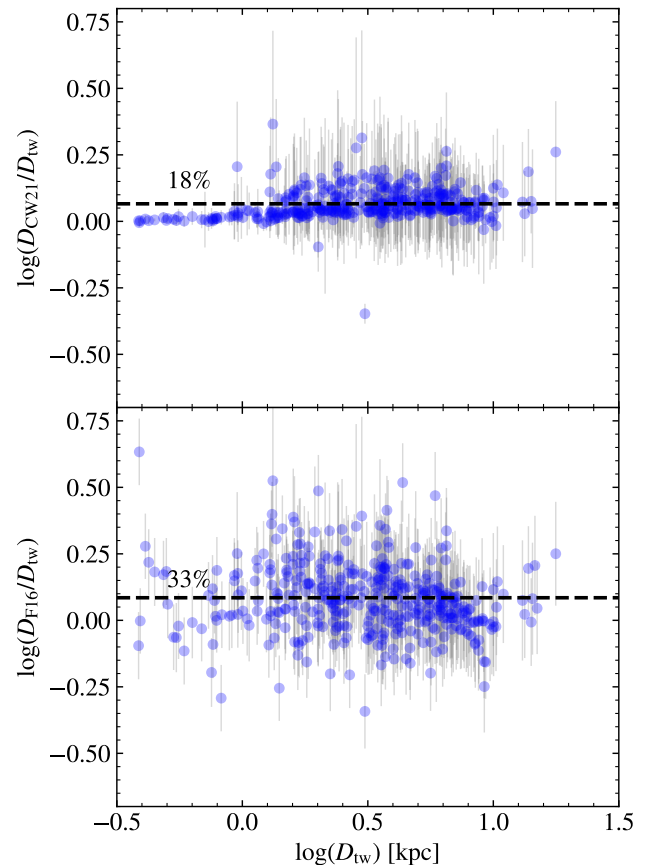

Figure 5. Top panel: Comparison between heliocentric distances derived from this work (D_{tw}) using the Bayesian approach and the ratio of the heliocentric distances from Chornay & Walton (2021) and this work, in logarithm for a better visualization. Bottom panel: the same as in the top panel but for F16 distances. In both panels the horizontal dashed lines indicate the average difference in the compared distances: 18% for CW21 and 33% for F16.

2.4. *Oxygen abundances*

The oxygen abundances used in this work are from Stanghellini & Haywood (2018) and BS23. They compiled a large set of chemical abundances from the literature and recalculate them using the same set of ionization correction factor (ICF) from Kingsburgh & Barlow (1994). While the recalculation of the chemical abundances with the same set of ICF is essential, we sill expect some dispersion of the data due to differences in the atomic data used by the different authors. For O^{++} the expected average abundance differences are of the order of 0.01 dex, with some larger divergences of 0.05 dex (see Stanghellini & Haywood 2018).

As PNe are the product of the evolution of 1–8 M$_\odot$ stars, the α-elements abundances are not expected to be modified during the evolution of the progenitor stars, reflecting the conditions of the ISM at the time the pro-
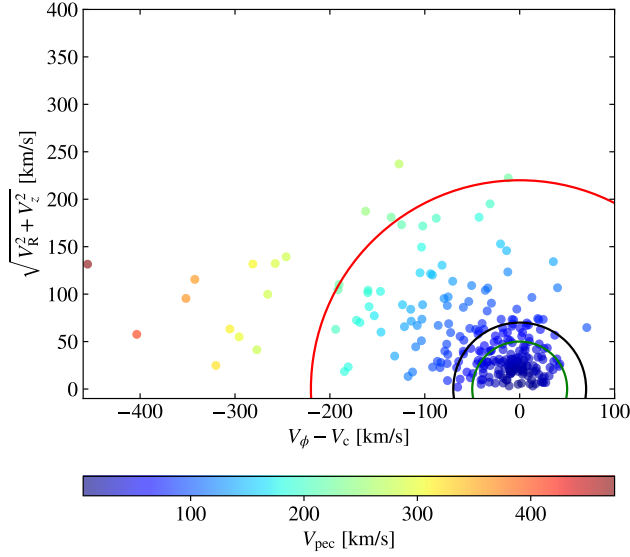
Figure 6. Toomre diagram to identify halo, thin and thick disks PNe. Green, black and red semi-circles show constant values of the total Galactic velocities of 50, 70, and 220 km/s. The data are color-coded using the V_{pec} velocities.

genitors were formed. However, for oxygen a small production or depletion may be observed due to both the dredge-up episodes and the hot-bottom burning during the AGB phase (Ventura et al. 2015), that depend on the metallicity and the mass of progenitor star. The modifications may be more relevant for the most massive progenitor stars, which are rare in the PNe population (see a discussion by Stanghellini et al. 2024). Therefore, the expected modifications in oxygen abundances in PNe are lower than the current uncertainties in the chemical abundances and we can consider oxygen as a proxy of the ISM metallicity. To derive the radial abundance gradients, we consider the oxygen abundance ratio O/H, which has been derived for a large number of objects in the Galaxy and has the smallest uncertainties among all known abundances.

3. RESULTS

The results reported in the previous section are summarized in Table 2, where we provide the *Gaia* source identification and the obtained parameters from DR3, the statistical distances calculated with the recalibrated Hα surface brightness–radius relation and also the Bayesian distances. The peculiar velocities V_{pec} are also reported in the table. A description for each column of the table is provided as a note. We recommend to use the Bayesian distances when available and the statistical distances otherwise.

Table 2. *Gaia* DR3 source identification and catalog of distances.

PNG	Name	ℓ	b	Source ID	RA_{DR3}	DE_{DR3}	G	$G_{BP} - G_{RP}$	ϖ	RUWE	Case	D_{stat}	D_{B}	V_{pec}
		(°)	(°)		(°)	(°)	(mag)	(mag)	(mas)			(pc)	(pc)	(km/s)
(a)	(b)	(c)	(d)	(e)	(f)	(g)	(h)	(i)	(j)	(k)	(l)	(m)	(n)	(o)
000.0-06.8	H 1-62	360.000	-6.850	4045771305065496576	273.325	-32.329	14.36	0.10	0.090 ± 0.034	0.78	B	6108 ± 2430	8478^{+1593}_{-1271}	190.7 ± 35.5
000.1+17.2	PC 12	0.164	17.269	...	...	...	...	...	...	...	...	8670 ± 3390	...	...
000.1-01.7	PHR J1752-2941	0.153	-1.738	4056406052047489024	268.205	-29.699	19.24	...	4.207 ± 1.135	1.02	B	5317 ± 2540	...	...
000.1-02.3	Bl 3-10	0.205	-2.342	...	...	...	...	...	...	...	...	7434 ± 3240	...	...
000.0-06.8	H 1-62	360.000	-6.850	4045771305065496576	273.325	-32.329	14.36	0.10	0.090 ± 0.034	0.78	B	6108 ± 2430	8478^{+1593}_{-1271}	190.7 ± 35.5
000.1+17.2	PC 12	0.164	17.269	...	...	...	...	...	...	...	...	8670 ± 3390	...	...
000.1-01.7	PHR J1752-2941	0.153	-1.738	4056406052047489024	268.205	-29.699	19.24	...	4.207 ± 1.135	1.02	B	5317 ± 2540	...	...
000.1-02.3	Bl 3-10	0.205	-2.342	...	...	...	...	...	...	...	...	7434 ± 3240	...	...
000.1-05.6	H 2-40	0.154	-5.616	4049045783774253568	272.128	-31.610	18.46	0.60	0.362 ± 0.268	1.25	C	4695 ± 1990	...	...
000.2+01.7	JaSt 19	0.284	1.719	4060845330160399360	264.914	-27.790	18.64	-0.55	-0.537 ± 0.262	1.12	A	6938 ± 2490	...	...
000.2+06.1	Terz N 67	0.228	6.154	4109954093684907008	260.722	-25.418	19.35	...	0.068 ± 0.522	0.97	C	7253 ± 3270	...	...
000.2-01.9	M 2-19	0.230	-1.930	4056495151130724352	268.440	-29.730	16.88	-0.45	-0.137 ± 0.112	1.19	A	4115 ± 1550	...	...
000.3+12.2	IC 4634	0.362	12.215	4126115570219432448	255.390	-21.826	13.85	-0.65	0.391 ± 0.043	0.62	A	2429 ± 790	2591^{+278}_{-205}	53.0 ± 6.5
000.3-01.6	PHR J1752-2930	0.330	-1.647	4056552085238266368	268.217	-29.501	16.68	0.74	0.375 ± 0.079	0.98	C	8370 ± 3480	...	...

NOTE—Table 2 is published in its entirety in the machine-readable format. A portion is shown here for guidance regarding its form and content. The columns of the table correspond to the following identifications: (a) PN PNG number; (b) PN name; (c) PN Galactic longitude; (d) PN Galactic latitude; (e) *Gaia* DR3 source identification (f) *Gaia* right ascension coordinate in degrees; (g) *Gaia* declination coordinate in degrees; (h) *Gaia* G magnitude; (i) *Gaia* extinction corrected color; (j) *Gaia* parallax corrected; (k) *Gaia* RUWE parameter; (l) identification case; (m) statistical distance in parsec; (n) Bayesian distance in parsec; (o) peculiar velocity in km/s.
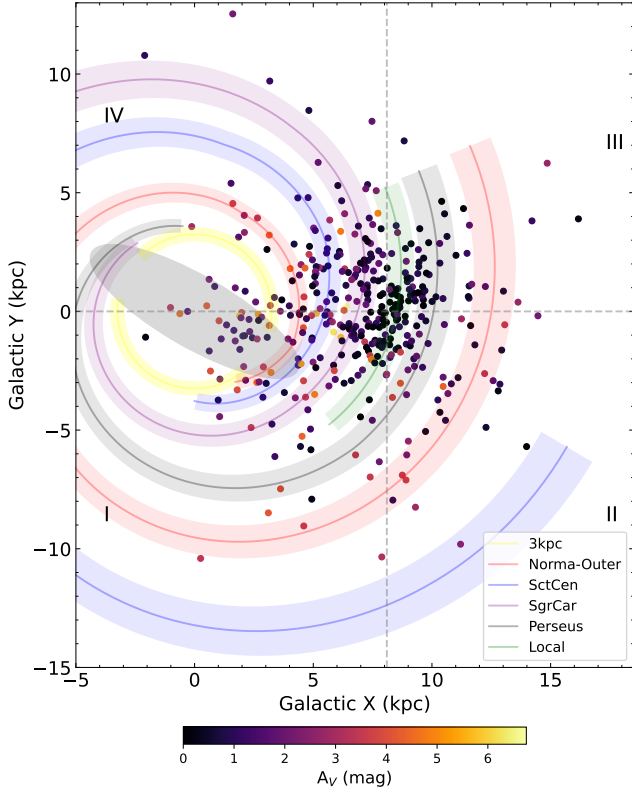
Figure 7. Distribution of the 419 PNe in the Galactic plane as seen from top view and using our Bayesian distances calculated in Section 2.2.2. The color bar indicates the interstellar extinction (A_V) as described in Section 2. The Milky Way spiral arms positions are from Reid et al. (2019) and the names are given at the bottom right. The shaded ellipse near the center represent the position of the Galactic bar after Wegg et al. (2015). The location of the Sun is marked by the interception of the dashed lines at (8.1,0.0) and the Galactic Center is located at (0,0). The Galactic quadrants are marked using roman numerals.

3.1. *2D distribution of the PNe in the Galactic plane*

The distances derived in this work can be used to study the 2D distribution of the PNe in the Galactic plane. In Fig. 7, the distribution of the PNe in the Galactic plane is plotted and, in order to interpret the distribution, the spiral arms and the Galactic bar positions are over-plotted in the figure, as described in the caption. It is possible to see a good correspondence between the PNe distribution and the expected positions of the spiral arms and the Galactic bar.

Most of the PNe likely have ages < 4 Gyr (Maciel & Costa 2013) and, therefore, they are not expected to be tracers of the spiral arms. However, as seen in Fig. 7, some PNe are located in the spiral arms, as well as in the bulge/bar region. Beyond the Galactic Center, in the I and IV quadrants, we cannot obtain distances

for the PNe using the Bayesian method, because the parallaxes for these sources cannot be measured. In the figure some radial migration can be seen, specially in the outer regions in the II and III quadrants. The data also capture the the higher interstellar extinction in the direction of the central regions of the Galaxy, meanwhile in the solar neighborhood the extinctions are lower. The distribution of PNe in Fig. 7 makes us confident that the Bayesian distances derived in this work are one of the best PNe distances available to study the radial chemical abundance gradients in the Milky Way.

3.2. *Radial oxygen abundance gradients*

One of the most important aspects in deriving accurate distances for Galactic PNe is to study the radial metallicity gradients in the Galaxy. For this purpose, and to obtain the metallicity gradient for a large Galactocentric distance interval using as many as PNe with accurate chemical abundances available, in this Section we will use the Bayesian distances whenever possible, combined with the new statistical distances obtained with the recalibration of the Hα surface brightness–radius relation. This way, most of the nearest PNe have more accurate distances, based on *Gaia* parallaxes, while the farthest PNe have distances derived using the statistical distances. As an additional step, the heliocentric distances derived in this work were converted to Galactocentric distances R using the `Astropy` package.
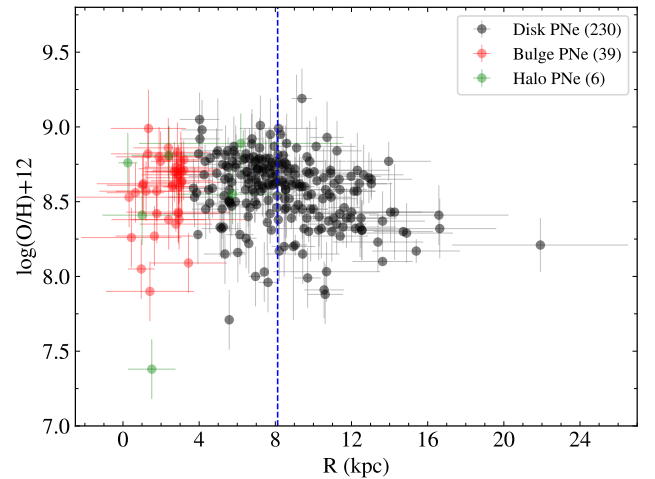
Figure 8. Radial abundance distribution for oxygen including all objects in our sample. The PNe were classified as disk, bulge and halo with the number of PNe in each population indicated in parenthesis, as labeled. The vertical dashed line marks the Sun position at 8.122 kpc.

The radial O/H distribution is shown in Fig. 8, where the PNe were separated in those pertaining to the disk (230 PNe), bulge (39 PNe) or halo (6 PNe) populations.

As in BS23, the halo population was selected by those PNe with $V_{pec} > 220$ km/s. The bulge PNe were selected as those PNe with $R < 3.5$ kpc and are in the direction of the Galactic Center with Galactic coordinates $335° < \ell < 25°$ and $|b| < 25°$. The remain PNe were classified as disk population.

Interestingly, inside the solar radius the data show a flat distribution, while outside the solar radius there is a decrease in the the abundances as the Galactocentric distances increase, until ~ 14 kpc, where the abundance distribution seems to become flat again.

In order to provide a more objective gradient fitting procedure, we will employ in this work the same methodology as in Cardoso et al. (2025), where a detailed analysis of the O/H radial abundance gradients derived from the H II region is performed in 154 isolated spiral galaxies observed by the CALIFA survey. The problem of gradient fitting is addressed using a robust unsupervised automatic fitting procedure that employs a bootstrap process on the data to escape local minima. To perform the fit of the abundance radial gradient, we use the Python package `piecewise regression` (Pilgrim 2021). This method simultaneously fits breakpoints positions and linear models for the different fit segments and gives confidence intervals for all the model estimates. The chosen models are a simple linear fit and piecewise linear functions presenting one or two breaks in the radial distributions.

Fig. 9 shows the results of the fitted models and Table 3 summarizes the parameters. In this table the columns refer to the model (linear, one-break and two-break) and the lines the fitted parameters. In the case of the linear model, a_1 and b_1 represent the slope and the intercept. For the one-break and two-break models they represent the parameters of the first segment. a_2 is the slope of the second segment for the one-break and two-break models and a_3 is the slope of the third segment for the two-break model.

To decide between the models, the Akaike information criterion (AIC, Akaike 1973) is adopted. We refer to Cardoso et al. (2025) and references therein for more information. The second to last row of Table 3 presents the AIC values for each of the fitted models. The most probable model is the one with one break in the radial distribution, presenting the lowest AIC value. In this case, there is a break in the radial distribution at 7.84 ± 1.40 kpc, close to the solar radius. Both models with one and two breaks indicate a flatter gradient inside the solar radius, while outside the solar radius the gradient is steeper. For the one-break model the slopes are 0.009 ± 0.025 and -0.035 ± 0.01 dex/kpc, for the first and second segments, respectively. The two-

Table 3. Parameters of the fitted models.

| Parameters | Model | | |
| | Linear | One-break | Two-break |
(1)	(2)	(3)	(4)
a_1 (dex/kpc)	-0.021 ± 0.006	0.009 ± 0.025	0.012 ± 0.017
a_2 (dex/kpc)	$\cdots$	-0.035 ± 0.010	-0.078 ± 0.112
a_3 (dex/kpc)	$\cdots$	$\cdots$	-0.024 ± 0.017
b_1 (dex)	8.74 ± 0.05	8.54 ± 0.15	8.53 ± 0.11
h_1 (kpc)	$\cdots$	7.84 ± 1.40	8.33 ± 1.30
h_2 (kpc)	$\cdots$	$\cdots$	9.78 ± 1.70
AIC	31.32	29.23	30.08
$\mathcal{L}(m_i|x)$	0.35	1	0.65

break model has slopes 0.012 ± 0.017, -0.078 ± 0.112 and -0.024 ± 0.017 dex/kpc, for the first, second and third segments, respectively. In this case, the second segment is the steepest, however with a very short radial range of about 1.5 kpc. Therefore, in this case there is a step in the radial O/H abundance distribution near the Sun position.

The likelihood of a model given the data $\mathcal{L}(m_i|x)$ calculated based on the IAC values (Burnham & Anderson 2002) are presented in the last row of Table 3, where the minimum AIC model is taken as reference. The alternative models have $\mathcal{L}(m_i|x) > 0.05$, so that the current PNe data do not allow to infer which of the models are the best to fit the data. For this, we need data with smaller uncertainties both in the chemical abundances and distances to confirm the change in slope of the radial O/H gradient near the solar radius.

3.3. Azimuthal variations in the metallicity distribution

To investigate the azimuthal structure in the metallicity distribution, we adopted a procedure similar to Wenger et al. (2019, and references therein). They analyzed the metallicity structure in the Galactic disk from H II regions and using the software package `pyKrige`[5], which employs kriging (see Feigelson & Babu 2012), to interpolate the distribution of oxygen abundances and to produce an abundance map in the Galactic plane. This technique is particularly suitable for PNe, since their distribution across the Galactic disk is sparse and irregular, and kriging provides an unbiased and variance-minimizing interpolation under such conditions. To interpolate the data we define a grid of Galactic coordinates in the plane ranging from -12 to 12 kpc in the x-direction and from -4 to 20 kpc in the y-direction in

---

[5] See https://github.com/bsmurphy/PyKrige.
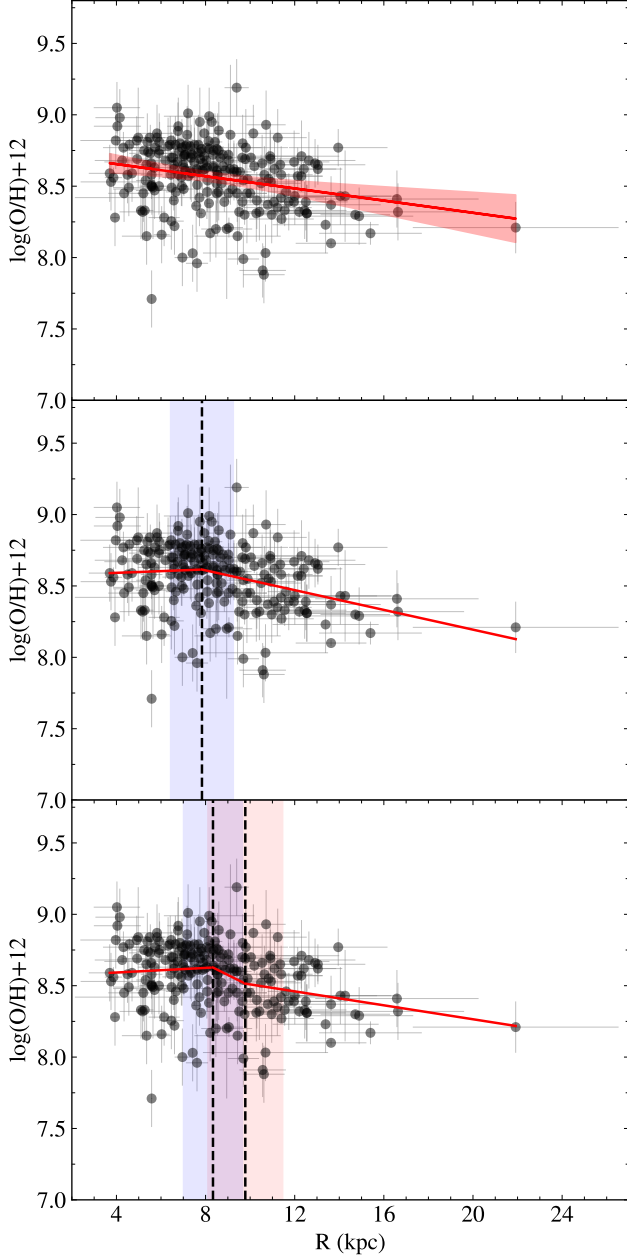
Figure 9. Radial O/H gradient for disk PNe. Top panel: a simple linear fit with the shaded region representing the 95% confidence interval (linear model). Middle panel: a fit considering a break in the radial distribution (one-break model). Bottom panel: a fit with two breaks (two-break model). The vertical dashed lines mark the position of the breaks and the shaded regions the 68% confidence interval.

steps of 1 kpc. To generate an error map to access the uncertainties in the procedure, a Monte Carlo simulation was implemented, which consists of generating random Gaussian values in the distances and abundances within their uncertainties. We adopted 500 Monte Carlo realizations, generating in this way for each simulation a

kriging map using a linear semivariogram model. Then, for each cell of the grid in the Galactic plane, we construct a PDF of the interpolated values and fit a KDE to the abundance distributions. The adopted interpolation value of abundance is the peak of the fitted KDE and the 1-σ confidence interval is represented by the bounds of the distribution that encompass 68% of the PDF area.

The results are shown in Fig. 10, where in the top panel the O/H abundance map is presented in a face-on view of the Galactic plane and in the bottom panel the respective error map in the O/H abundances. The differences in the interpolated chemical abundances in the O/H map are not very large, but the map revels an azimuthal asymmetry in the distribution. The abundances are higher near the solar circle and near the Galactic Center at positive longitudes. The higher abundances near $X = 0$ and $Y = 5$ kpc seem to coincide with end of the expected position of the Galactic bar. This asymmetry in the abundance distribution was also noted by Gaia Collaboration et al. (2023a) using stellar chemical abundances from *Gaia* DR3 data and may be related to radial gas flows induced by the Galactic bar from the OLR to the bar corotation radius, as predicted by chemical evolution models (Cavichia et al. 2014; Kubryk et al. 2015). In the O/H map it is also possible to detect the radial O/H abundance gradient, as beyond the solar circle the abundances drop continuously. The solar circle appears to be a transition region in the pattern of chemical abundance distribution. Inside the solar circle the abundances are higher than in the outside region, creating a bimodal pattern of chemical abundance distribution. This characteristic is consistent with the fits obtained in the one-break and two-break models presented in Fig. 9, where breaks in the radial distribution are detected near the solar circle.

3.4. *Thin and thick disk O/H radial gradients*

To further investigate O/H radial gradient in the Galaxy, we separate the disk PNe in the Toomre diagram (see Fig. 6) into those pertaining to the thin disk ($V_{pec} < 50$ km/s) and to the thick disk ($70 < V_{pec} < 220$ km/s), as suggested by Bensby et al. (2014). The top panel of Fig. 11 shows the O/H radial gradient including all objects in our sample with measured V_{pec}. In the middle panel, the O/H radial gradient for PNe is depicted from the thin disk, and in the bottom panel the radial gradient for the thick disk PNe. Table 4 lists the following results of the performed linear fits: the sample name; the number of objects in each sample; slope and respective error; and intercept and respective error. The thin disk O/H radial gradient obtained in this work is steeper than that of the thick disk and more in
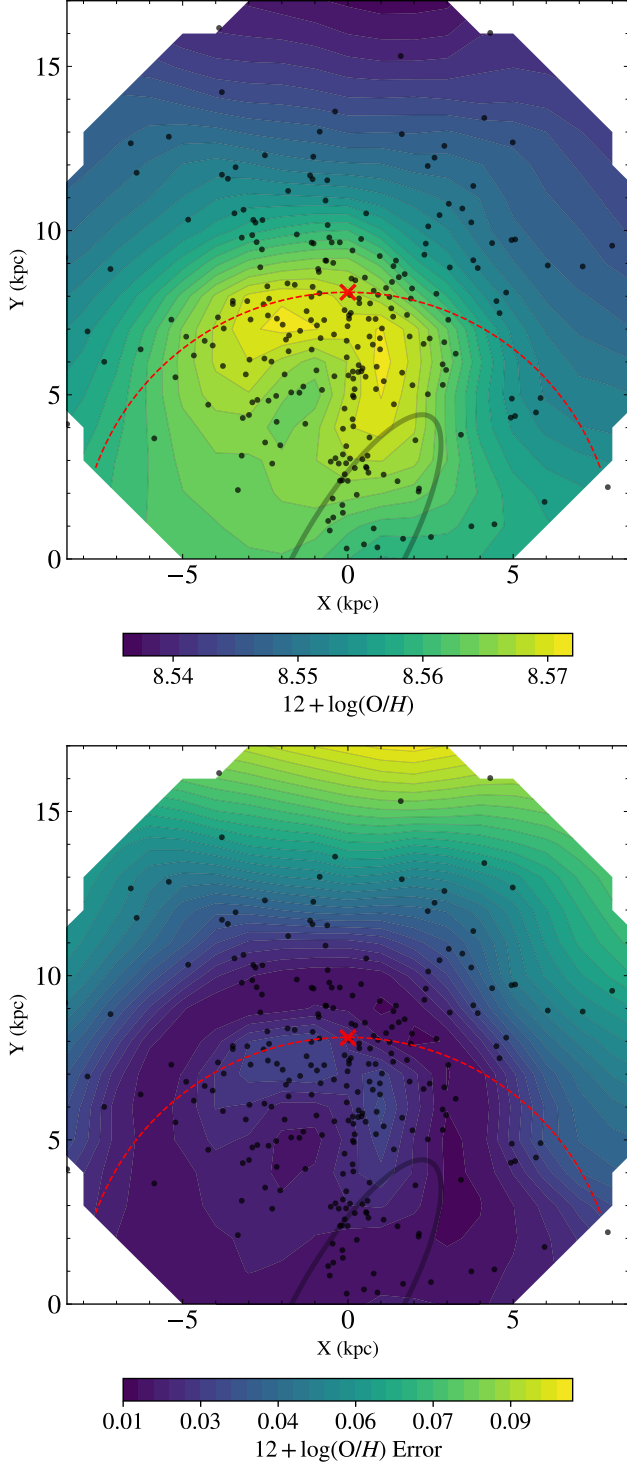
Figure 10. Top: the $\log(O/H) + 12$ abundance map interpolated using the 2D universal kriging algorithm. Bottom: the respective $\log(O/H) + 12$ error map. In both panels the red x marks the position of the Sun and the red dashed semicircunference the solar radius. The gray ellipse centered in the origin represent the position of the Galactic bar after Wegg et al. (2015).

Table 4. Radial O/H gradients for PNe with $V_{\rm pec}$.

Sample	N	Slope (dex/kpc)	Intercept (dex)
(1)	(2)	(3)	(4)
All	100	-0.018 ± 0.008	8.75 ± 0.07
Thin	54	-0.036 ± 0.011	8.93 ± 0.11
Thick	24	-0.012 ± 0.015	8.68 ± 0.10

NOTE—In this table the radial O/H gradients are calculated using only disk PNe with measured peculiar velocities $V_{\rm pec}$.

agreement with that of the H II regions (e.g. Esteban & García-Rojas 2018; Esteban et al. 2017). In particular, Arellano-Córdova et al. (2020) the obtained a slope of -0.037 ± 0.009 dex/kpc for disk H II regions using distances based on *Gaia* DR2 data, which is in excellent agreement with the one obtained here for the thin disk.

Additionally, the dispersion of the data around the linear relation for thin-disk PNe is lower than considering all-disk PNe as in Fig. 9. The selection of PNe with lower values of $V_{\rm pec}$ implies an age criterion, since younger objects tend to follow the Galactic rotation curve closer (Maciel et al. 2011). The dispersion of the data around the linear relation seen in the top panel of Fig. 9 may be an effect of the chemical evolution of the Galaxy, as probably the range of ages of the progenitors of the PNe are much higher, increasing the dispersion in the abundances. Additionally, the radial migration of the progenitor stars may also affect the dispersion, contributing to mixing PNe from different radii in the Galaxy and, therefore, different chemical abundances. However, separating both effects is out of the scope of this paper. The O/H radial gradient for thick disk PNe is shallower than that of thin disk, and there is a large number of PNe within the solar radius ($R < 8$ kpc). Such a feature was also observed by BS23, however, they use a chemical abundance criterion to classify older and younger PNe, which relies on models of stellar evolution and is subject to the related uncertainties. As can be seen in their figure 8, the younger sample has a higher scatter of the data around the linear relation, and the gradient is shallower than the thin disk PNe obtained in this work.

4. DISCUSSION AND CONCLUSIONS

A long-standing discussion regarding the radial abundance gradient from PNe concerns the constancy of its
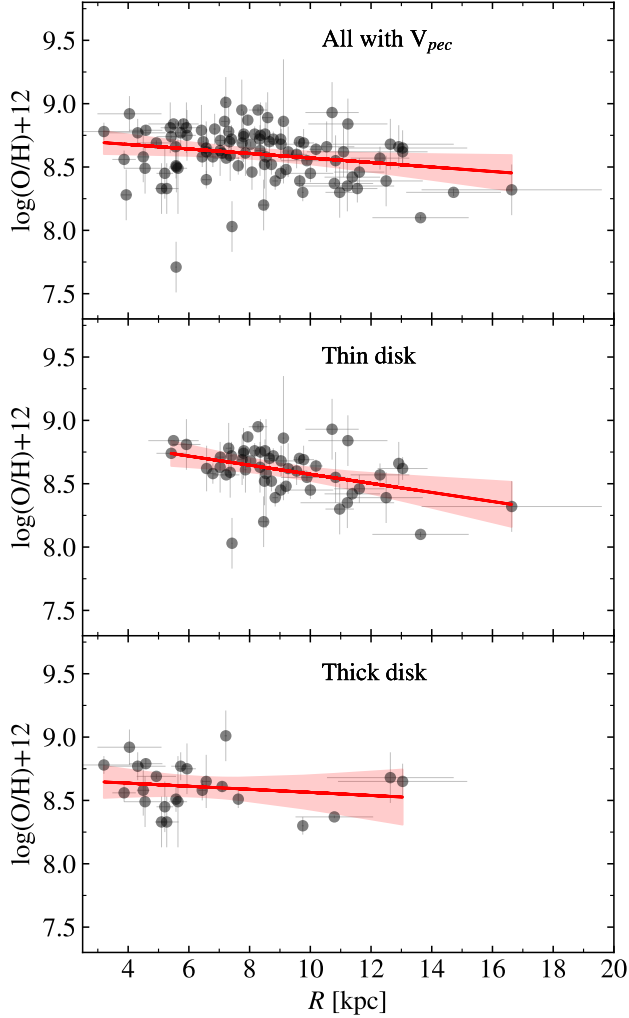
Figure 11. Radial abundance gradient for oxygen including all disk PNe with calculated V_{pec}, thin and thick disks PNe, in top, middle and bottom panels, respectively. In each panel the red line is the single linear fit and the shaded region the 95% confidence interval.

slope across the Galactic disk. Previous results suggest either a flattening of the oxygen gradient at large Galactocentric distances (e.g., Maciel & Costa 2009; Stanghellini & Haywood 2018) or, conversely, a steepening (e.g., Henry et al. 2010). Part of this disagreement arises from the different methods used to estimate the PN distances. To address this issue, in this work, we provide a recalibration of the Hα surface brightness–radius relation from F16, based on *Gaia* DR3 data, to derive statistical distances for 1,200 Galactic PNe. In addition, Bayesian distances are provided for a smaller sample of 440 PNe with available *Gaia* parallaxes. Using these distances, adopting the Bayesian method preferentially and the statistical method otherwise, we derived the O/H radial gradient for a sample of 230 disk PNe.

We present the two-dimensional distribution of PNe in the Galactic plane and compare it with the expected locations of the spiral arms and the Galactic bar. The distribution shown in Fig. 7 supports the reliability of the Bayesian distances derived in this work, indicating that they are among the most robust PNe distances currently available to investigate the radial chemical abundance gradients in the Milky Way.

The O/H radial gradient derived for the disk PNe sample using segmented fit exhibits a significant break near the solar region, as revealed by segmented linear models. These fits, incorporating one or two radial breaks, indicate a flatter, or even slightly positive, gradient in the inner disk for $R \lesssim 8\,\mathrm{kpc}$. Beyond this radius, the gradient transitions to a steeper and more negative slope compared to a single linear fit. This potential change of slope in the radial gradient at $R \approx 8\,\mathrm{kpc}$ deserves further investigation. However, according to the Akaike Information Criterion (AIC), the selection of the best model between a single linear fit, a segmented fit with one break, and a segmented fit with two breaks, is inconclusive, implying that all three are plausible given the current data. The single linear fit for disk PNe resulted in a slope of -0.021 ± 0.006 dex/kpc, in agreement with the most recent O/H radial gradient from PNe (Bucciarelli & Stanghellini 2023; Stanghellini & Haywood 2018).

The results found in this work are generally consistent with previous findings in the literature. The flattening observed in Cepheids (Martin et al. 2015; Andrievsky et al. 2016) and in red giants (Hayden et al. 2014) appears to occur at smaller Galactocentric radii ($R \sim 5$–6 kpc). The findings of Esteban et al. (2017); Esteban & García-Rojas (2018) using H II regions are consistent with the evidence from PNe reported here. Stanghellini & Haywood (2018) proposed that the O/H radial distribution for disk PNe may be best described by a step function near $R \sim 10$ kpc rather than a continuous gradient. Their results are similar to those presented here, but with important differences. We also find that the O/H gradient is flatter, or even positive, in the inner Galaxy; however, the transition region is closer to the Sun, at $R \sim 8$ kpc. Another significant difference concerns the gradient in the outer Galaxy, which remains negative and is steeper in both the one-break and two-break models than their suggested gradient. It is also worth noting that Stanghellini & Haywood (2018) derived their results by fitting the radial O/H distribution by imposing the step function manually, whereas our analysis is based on well-defined statistical criteria and a robust and automatic fitting procedure.

Although statistically we cannot favor a single model, our results are qualitatively consistent with a change of

slope in the O/H radial gradient. The existence of two distinct gradient slopes is often attributed to variations in gas infall and star formation rates between the inner and outer disk. One possible explanation for the change in slope is a quenching of star formation efficiency caused by the dynamical action of the Galactic bar (see Esteban & García-Rojas 2018, for a discussion). Simulations show that the non-axisymmetric gravitational potential of the bar drives gas inflows toward the central regions of galaxies (e.g. Fragkoudi et al. 2016, and references therein), and observations confirm bar-driven gas transport (e.g. López-Cobá et al. 2022, and references therein). According to the chemical evolution model (CEM) of the Milky Way by Cavichia et al. (2014), the bar induces radial gas flows within the corotation radius, increasing gas density while diluting abundances, and simultaneously enhancing the star formation rate. Carigi et al. (2019) proposed a CEM in which the flattening of the oxygen gradient in the inner Galaxy arises from inside-out quenching of the star formation history. The origin of this quenching may be gas flows toward the Galactic Center induced by the bar.

Another possibility is that the break in the O/H radial gradient is related to the corotation resonance of the spiral pattern. It has been suggested that the Galaxy undergoes a bimodal chemical evolution, since gas kinematics has opposite directions at the corotation radius. Using a homogeneous open cluster sample with *Gaia* DR2 data, Dias et al. (2019) determined the corotation radius to be located at 8.51 ± 0.64, kpc, close to the solar orbit. This value agrees with the break in the O/H gradient derived from PNe in this work. Breaks in the abundance gradient near the corotation radius have been reported by many authors using different tracers (e.g., Carney et al. 2005; Lépine et al. 2011; Genovali et al. 2014; Reddy et al. 2016; Stanghellini & Haywood 2018; Monteiro et al. 2021; Magrini et al. 2023; Yang et al. 2025). However, Reddy et al. (2016) argued that the change in slope may instead reflect a mixture of stellar populations at different vertical distances from the Galactic plane: Clusters close to the mid-plane trace a steeper radial metallicity gradient, whereas those located farther away trace a shallower one. This is consistent with the results obtained in this work for PNe when comparing the O/H radial gradients of the thin and thick disks, with the thin-disk PNe showing a steeper gradient.

Breaks in the O/H radial gradient have also been reported in other spiral galaxies (Sánchez et al. 2014; Sánchez-Menguiano et al. 2016, 2018; Easeman et al. 2022; Pilyugin & Tautvaišienė 2024; Cardoso et al. 2025). In particular, Sánchez-Menguiano et al. (2018) analyzed the O/H radial distribution of H II regions in a sample of 102 spiral galaxies observed with VLT/MUSE and detected a characteristic break at $\sim 1.5\,R_{\rm e}$, although with significant variation among individual galaxies. Adopting an effective radius of $R_{\rm e} = 5.85\,{\rm kpc}$ for the Milky Way (Mollá et al. 2019), $1.5\,R_{\rm e}$ corresponds to $\sim 8.8\,{\rm kpc}$, which is consistent with the position of the breaks suggested by both the one-break and two-break models derived in this work.

To investigate the O/H azimuthal distribution in the Galactic plane, we applied a kriging interpolation algorithm. The results reveal an azimuthal asymmetry, with higher abundances near the bar position at positive longitudes. However, the abundance variations are modest and remain within the measurement uncertainties. In the O/H map it is also possible to note the bimodal abundance pattern for the inner and outer solar regions. The azimuthal metallicity structure of the Milky Way has also been studied using H II regions (e.g., Balser et al. 2011, 2015; Wenger et al. 2019). These works report differences of up to a factor of two in the O/H radial gradient depending on the azimuthal angle considered. Similarly to our results, the O/H maps from Balser et al. (2015); Wenger et al. (2019) show enhanced abundances near the Galactic bar at positive longitudes. However, their analysis lacks H II regions in the third and fourth Galactic quadrants, preventing a direct comparison with the results obtained here.

The findings obtained in this work emphasize the complex interplay between Galactic dynamics, star formation, and chemical evolution, highlighting the importance of considering both radial and azimuthal variations in abundance studies. Future work combining larger, homogeneous samples with improved distance and abundance determinations will be essential to confirm the presence and origin of the observed gradient break and to refine models of Galactic chemical evolution.

cosmos.esa.int/web/gaia/dpac/consortium). Funding
for the DPAC has been provided by national institu-
tions, in particular the institutions participating in the
Gaia Multilateral Agreement.

Software: Astropy (Astropy Collaboration et al.
2022), Matplotlib (Hunter 2007), NumPy & SciPy (Vir-
tanen et al. 2020), PyKrige (Murphy 2014), Python
(https://www.python.org/).

REFERENCES

Acker, A., Marcout, J., Ochsenbein, F., Stenholm, B., &
Tylenda, R. 1992, Strasbourg - ESO catalogue of galactic
planetary nebulae. Part 1; Part 2 (Garching: European
Southern Observatory)

Akaike, H. 1973, Akadémiai Kiadó, Budapest

Ali, A., Algarni, E., Mindil, A., & Alghamdi, S. A. 2022,
Research in Astronomy and Astrophysics, 22,
doi: 10.1088/1674-4527/ac7545

Andrievsky, S. M., Martin, R. P., Kovtyukh, V. V.,
Korotin, S. A., & Lépine, J. R. D. 2016, MNRAS, 461,
4256, doi: 10.1093/mnras/stw1631

Arellano-Córdova, K. Z., Esteban, C., García-Rojas, J., &
Méndez-Delgado, J. E. 2020, MNRAS, 496, 1051,
doi: 10.1093/mnras/staa1523

Astropy Collaboration, Price-Whelan, A. M., Lim, P. L., &
et al. 2022, ApJ, 935, 167, doi: 10.3847/1538-4357/ac7c74

Bailer-Jones, C. A. L. 2015, PASP, 127, 994,
doi: 10.1086/683116

Bailer-Jones, C. A. L., Rybizki, J., Fouesneau, M.,
Demleitner, M., & Andrae, R. 2021, AJ, 161, 147,
doi: 10.3847/1538-3881/abd806

Balser, D. S., Rood, R. T., Bania, T. M., & Anderson, L. D.
2011, ApJ, 738, 27, doi: 10.1088/0004-637X/738/1/27

Balser, D. S., Wenger, T. V., Anderson, L. D., & Bania,
T. M. 2015, ApJ, 806, 199,
doi: 10.1088/0004-637X/806/2/199

Bensby, T., Feltzing, S., & Oey, M. S. 2014, A&A, 562,
A71, doi: 10.1051/0004-6361/201322631

Bresolin, F., Ryan-Weber, E., Kennicutt, R. C., &
Goddard, Q. 2009, ApJ, 695, 580,
doi: 10.1088/0004-637X/695/1/580

Bucciarelli, B., & Stanghellini, L. 2023, A&A, 680, A104,
doi: 10.1051/0004-6361/202347519

Bundy, K., Bershady, M. A., Law, D. R., & et al. 2015,
ApJ, 798, 7, doi: 10.1088/0004-637X/798/1/7

Burnham, K., & Anderson, D. 2002, Model Selection and
Multimodel Inference : A Practical Information-Theoretic
Approach, 2nd edn. (New York, NY: Springer New York :
Imprint: Springer)

Cardoso, A. F. S., Cavichia, O., Mollá, M., &
Sánchez-Menguiano, L. 2025, ApJ, 980, 45,
doi: 10.3847/1538-4357/ad9eab

Carigi, L., Peimbert, M., & Peimbert, A. 2019, ApJ, 873,
107, doi: 10.3847/1538-4357/aaf28e

Carney, B. W., Yong, D., Teixera de Almeida, M. L., &
Seitzer, P. 2005, AJ, 130, 1111, doi: 10.1086/432541

Cavichia, O., Mollá, M., Costa, R. D. D., & Maciel, W. J.
2014, MNRAS, 437, 3688, doi: 10.1093/mnras/stt2164

Chornay, N., & Walton, N. A. 2020, A&A, 638, A103,
doi: 10.1051/0004-6361/202037554

—. 2021, A&A, 656, A110,
doi: 10.1051/0004-6361/202142008

Dias, W. S., Monteiro, H., Lépine, J. R. D., & Barros, D. A.
2019, MNRAS, 486, 5726, doi: 10.1093/mnras/stz1196

Durand, S., Acker, A., & Zijlstra, A. 1998, A&AS, 132, 13

Easeman, B., Schady, P., Wuyts, S., & Yates, R. M. 2022,
MNRAS, 511, 371, doi: 10.1093/mnras/stac017

Esteban, C., Carigi, L., Copetti, M. V. F., et al. 2013,
MNRAS, 433, 382, doi: 10.1093/mnras/stt730

Esteban, C., Fang, X., García-Rojas, J., & Toribio San
Cipriano, L. 2017, MNRAS, 471, 987,
doi: 10.1093/mnras/stx1624

Esteban, C., & García-Rojas, J. 2018, MNRAS, 478, 2315,
doi: 10.1093/mnras/sty1168

Feigelson, E. D., & Babu, G. J. 2012, Modern Statistical
Methods for Astronomy, doi: 10.48550/arXiv.1205.2064

Fernández-Martín, A., Pérez-Montero, E., Vílchez, J. M., &
Mampaso, A. 2017, A&A, 597, A84,
doi: 10.1051/0004-6361/201628423

Fragkoudi, F., Athanassoula, E., & Bosma, A. 2016,
MNRAS, 462, L41, doi: 10.1093/mnrasl/slw120

Frew, D. J., Bojičić, I. S., & Parker, Q. A. 2013, MNRAS,
431, 2, doi: 10.1093/mnras/sts393

Frew, D. J., Parker, Q. A., & Bojičić, I. S. 2016, MNRAS,
455, 1459, doi: 10.1093/mnras/stv1516

Gaia Collaboration, Brown, A. G. A., Vallenari, A., Prusti,
T., & et al. 2018, A&A, 616, A1,
doi: 10.1051/0004-6361/201833051

Gaia Collaboration, Prusti, T., de Bruijne, J. H. J., Brown, A. G. A., & et al. 2016, A&A, 595, A1, doi: 10.1051/0004-6361/201629272

Gaia Collaboration, Recio-Blanco, A., Kordopatis, G., de Laverny, P., & et al. 2023a, A&A, 674, A38, doi: 10.1051/0004-6361/202243511

Gaia Collaboration, Vallenari, A., Brown, A. G. A., Prusti, T., & et al. 2023b, A&A, 674, A1, doi: 10.1051/0004-6361/202243940

Genovali, K., Lemasle, B., Bono, G., et al. 2014, A&A, 566, A37, doi: 10.1051/0004-6361/201323198

Gentile Fusillo, N. P., Tremblay, P. E., Cukanovaite, E., et al. 2021, MNRAS, 508, 3877, doi: 10.1093/mnras/stab2672

Gibson, B. K., Pilkington, K., Brook, C. B., Stinson, G. S., & Bailin, J. 2013, A&A, 554, A47, doi: 10.1051/0004-6361/201321239

González-Santamaría, I., Manteiga, M., Manchado, A., et al. 2021, A&A, 656, A51, doi: 10.1051/0004-6361/202141916

GRAVITY Collaboration, Abuter, R., Amorim, A., Anugu, N., & et al. 2018, A&A, 615, L15, doi: 10.1051/0004-6361/201833718

Green, G. M., Schlafly, E., Zucker, C., Speagle, J. S., & Finkbeiner, D. 2019, ApJ, 887, 93, doi: 10.3847/1538-4357/ab5362

Hayden, M. R., Holtzman, J. A., & et al. 2014, AJ, 147, 116, doi: 10.1088/0004-6256/147/5/116

Henry, R. B. C., Kwitter, K. B., Jaskot, A. E., Balick, B., & et al. 2010, ApJ, 724, 748, doi: 10.1088/0004-637X/724/1/748

Henry, R. B. C., & Worthey, G. 1999, PASP, 111, 919, doi: 10.1086/316403

Hernández-Juárez, D., Rodríguez, M., & Peña, M. 2024, RMxAA, 60, 227, doi: 10.22201/ia.01851101p.2024.60.02.03

Jordi, C., Gebran, M., Carrasco, J. M., et al. 2010, A&A, 523, A48, doi: 10.1051/0004-6361/201015441

Kimeswenger, S., & Barría, D. 2018, A&A, 616, L2, doi: 10.1051/0004-6361/201833647

Kingsburgh, R. L., & Barlow, M. J. 1994, MNRAS, 271, 257

Kubryk, M., Prantzos, N., & Athanassoula, E. 2015, A&A, 580, A127, doi: 10.1051/0004-6361/201424599

Lépine, J. R. D., Cruz, P., Scarano, Jr., S., et al. 2011, MNRAS, 417, 698, doi: 10.1111/j.1365-2966.2011.19314.x

Lindegren, L., Hernández, J., Bombrun, A., & et al. 2018, A&A, 616, A2, doi: 10.1051/0004-6361/201832727

Lindegren, L., Klioner, S. A., Hernández, J., & et al. 2021, A&A, 649, A2, doi: 10.1051/0004-6361/202039709

López-Cobá, C., Sánchez, S. F., Lin, L., et al. 2022, ApJ, 939, 40, doi: 10.3847/1538-4357/ac937b

Maciel, W. J., & Costa, R. D. D. 2009, in IAU Symposium, Vol. 254, IAU Symposium, ed. J. Andersen, Nordströara, B. m, & J. Bland-Hawthorn, 38P. https://arxiv.org/abs/0806.3443

Maciel, W. J., & Costa, R. D. D. 2013, RMxAA, 49, 333. https://arxiv.org/abs/1308.1884

Maciel, W. J., Costa, R. D. D., & Cavichia, O. 2015, RMxAA, 51, 165. https://arxiv.org/abs/1505.07640

Maciel, W. J., Rodrigues, T. S., & Costa, R. D. D. 2011, RMxAA, 47, 401, doi: 10.48550/arXiv.1108.5307

Magrini, L., Viscasillas Vázquez, C., Spina, L., & et al. 2023, A&A, 669, A119, doi: 10.1051/0004-6361/202244957

Marshall, D. J., Robin, A. C., Reylé, C., Schultheis, M., & Picaud, S. 2006, A&A, 453, 635, doi: 10.1051/0004-6361:20053842

Martin, R. P., Andrievsky, S. M., Kovtyukh, V. V., et al. 2015, MNRAS, 449, 4071, doi: 10.1093/mnras/stv590

McCall, M. L., Rybski, P. M., & Shields, G. A. 1985, ApJS, 57, 1, doi: 10.1086/190994

Méndez-Delgado, J. E., Amayo, A., Arellano-Córdova, K. Z., et al. 2022, MNRAS, 510, 4436, doi: 10.1093/mnras/stab3782

Minniti, J. H., Sbordone, L., Rojas-Arriagada, A., et al. 2020, A&A, 640, A92, doi: 10.1051/0004-6361/202037575

Mollá, M., Díaz, Á. I., Cavichia, O., & et al. 2019, MNRAS, 482, 3071, doi: 10.1093/mnras/sty2877

Monteiro, H., Barros, D. A., Dias, W. S., & Lépine, J. R. D. 2021, Frontiers in Astronomy and Space Sciences, 8, 62, doi: 10.3389/fspas.2021.656474

Murphy, B. S. 2014, in AGU Fall Meeting Abstracts, Vol. 2014, AGU Fall Meeting Abstracts, H51K–0753

Pagomenos, G. J. S., Bernard-Salas, J., & Pottasch, S. R. 2018, A&A, 615, A29, doi: 10.1051/0004-6361/201730861

Parker, Q. A., Acker, A., Frew, D., & et al. 2006, MNRAS, 373, 79, doi: 10.1111/j.1365-2966.2006.10950.x

Pilgrim, C. 2021, Journal of Open Source Software, 6, 3859, doi: 10.21105/joss.03859

Pilyugin, L. S., & Tautvaišienė, G. 2024, A&A, 682, A41, doi: 10.1051/0004-6361/202347032

Reddy, A. B. S., Lambert, D. L., & Giridhar, S. 2016, MNRAS, 463, 4366, doi: 10.1093/mnras/stw2287

Reid, M. J., Menten, K. M., Brunthaler, A., et al. 2019, ApJ, 885, 131, doi: 10.3847/1538-4357/ab4a11

Sánchez, S. F., Kennicutt, R. C., Gil de Paz, A., & et al. 2012, A&A, 538, A8, doi: 10.1051/0004-6361/201117353

Sánchez, S. F., Rosales-Ortega, F. F., Iglesias-Páramo, J.,
   & et al. 2014, A&A, 563, A49,
   doi: 10.1051/0004-6361/201322343

Sánchez-Menguiano, L., Sánchez, S. F., Pérez, I., & et al.
   2016, A&A, 587, A70, doi: 10.1051/0004-6361/201527450

—. 2018, A&A, 609, A119,
   doi: 10.1051/0004-6361/201731486

Schlegel, D. J., Finkbeiner, D. P., & Davis, M. 1998, ApJ,
   500, 525, doi: 10.1086/305772

Shaver, P. A., McGee, R. X., Newton, L. M., Danks, A. C.,
   & Pottasch, S. R. 1983, MNRAS, 204, 53

Smith, H. 2015, MNRAS, 449, 2980,
   doi: 10.1093/mnras/stv456

Stanghellini, L., Bucciarelli, B., Lattanzi, M. G., &
   Morbidelli, R. 2017, NewA, 57, 6,
   doi: 10.1016/j.newast.2017.06.004

—. 2020, ApJ, 889, 21, doi: 10.3847/1538-4357/ab59e4

Stanghellini, L., & Haywood, M. 2010, ApJ, 714, 1096,
   doi: 10.1088/0004-637X/714/2/1096

—. 2018, ApJ, 862, 45, doi: 10.3847/1538-4357/aacaf8

Stanghellini, L., Shaw, R. A., & Villaver, E. 2008, ApJ,
   689, 194, doi: 10.1086/592395

Stanghellini, L., Smith, V. V., Cunha, K., & Prantzos, N.
   2024, ApJ, 972, 130, doi: 10.3847/1538-4357/ad5963

Tylenda, R., Siódmiak, N., Górny, S. K., Corradi, R. L. M.,
   & Schwarz, H. E. 2003, A&A, 405, 627,
   doi: 10.1051/0004-6361:20030645

Ventura, P., Stanghellini, L., Dell'Agli, F.,
   García-Hernández, D. A., & Di Criscienzo, M. 2015,
   MNRAS, 452, 3679, doi: 10.1093/mnras/stv1590

Vila-Costas, M. B., & Edmunds, M. G. 1992, MNRAS, 259,
   121

Virtanen, P., Gommers, R., Oliphant, T. E., et al. 2020,
   Nature Methods, 17, 261, doi: 10.1038/s41592-019-0686-2

Wegg, C., Gerhard, O., & Portail, M. 2015, Monthly
   Notices of the Royal Astronomical Society, 450, 4050,
   doi: 10.1093/mnras/stv745

Weidmann, W. A., Mari, M. B., Schmidt, E. O., et al. 2020,
   A&A, 640, A10, doi: 10.1051/0004-6361/202037998

Wenger, T. V., Balser, D. S., Anderson, L. D., & Bania,
   T. M. 2019, ApJ, 887, 114,
   doi: 10.3847/1538-4357/ab53d3

Yang, G., Zhao, J., Yang, Y., et al. 2025, AJ, 169, 214,
   doi: 10.3847/1538-3881/adba45

Zaritsky, D., Kennicutt, Jr., R. C., & Huchra, J. P. 1994,
   ApJ, 420, 87, doi: 10.1086/173544